REVISION 1

H/D methane isotopologues dissolved in magmatic fluids: Stable hydrogen isotope fractionations in the Earth's interior

Dionysis I. Foustoukos and Bjorn O. Mysen

Geophysical Laboratory, Carnegie Institution of Washington, 5251 Broad Branch Rd. NW, Washington DC 20015

Keywords: condensed-phase isotope effect, methane, H/D isotopologues, supercritical water, magmatic fluids, Raman vibrational spectroscopy

ABSTRACT

A series of hydrothermal diamond anvil cell experiments was conducted to evaluate the role of supercritical water on the isotopic equilibrium between H/D methane isotopologues at 600 – 800 ^{o}C and 409 – 1622 MPa. Raman spectroscopy was deployed to investigate the distribution of H/D isotopic molecules formed during hydrothermal decomposition of $Si_5C_{12}H_{36}$ in H_2O-D_2O aqueous solutions. To this end, the intensities of the fundamental vibrational C-H and C-D modes of deuteromethanes were employed to determine the thermodynamic properties of isotope exchange reactions between H/D isotopologues and to constrain the methane D/H molar ratios. By adjusting the initial volume ratios of silane/H_2O-D_2O, reactions in the CH_4-D_2O-H_2O system were monitored for gaseous and supercritical-water phases. Discreet differences of the equilibrium constants describing the relationship between the CH_3D-CH_2D_2-CHD_3-CH_4 species dissolved in supercritical water or present as a homogeneous gas phase are revealed. The bulk D/H methane composition in the liquid- system is also twice that of the D/H molar ratios recorded in the gas-bearing system. Accordingly, condensed-phase isotope effects are inferred to play a key role on the evolution of H/D isotopologues, likely induced by

28 differences in the solubility of the isotopic molecules driven by the excess energy/entropy
29 developed during mixing of non-polar species in the H_2O-D_2O structure. Our experiments
30 show that isotope fractionation effects need to account for the presence of condensed
31 matter (e.g. melts, magmatic fluids), even at conditions at which theoretical models
32 suggest minimal (or nonexistent) isotope exchange, but comparable to those of the
33 Earth's interior.
34
35

INTRODUCTION

Theoretical studies on the distribution between and the equilibrium relationships of isotopic molecules are commonly based on statistical mechanics models that calculate the partition functions (rotational, translational, vibrational) of the molecules by adopting a Wigner-Kirkwood free energy expansion (Kirkwood, 1934; Wigner, 1932) and by assuming simple harmonic oscillators (Bigeleisen and Mayer, 1947; Bottinga, 1969). These methods adopt ideal gas behavior between species with zero intermolecular forces, and thus, do not account for solubility, molar volume, and vapor pressure induced fractionations imposed by intermolecular interactions with condensed phases such as, for example, supercritical water (Bacsik et al., 2002; Chialvo and Horita, 2003; Gomes and Grolier, 2001; Jancso et al., 1993; Muccitelli and Wen, 1978; Van Hook, 2006). Condensed-phase isotope effects are attributed to the free energy differences between the condensed and gas phase (Van Hook, 2006) as reflected, for example, in differences on the solution properties (e.g Henry's/Raoult's law) and/or the temperature and pressure dependence of isotopologues's vapor pressure and partial molar volumes (Bigeleisen, 2006; Herzfeld and Teller, 1938).

Silicate melts and coexisting magmatic fluids represent the condensed phases present in the Earth's interior. Determining the solubility and solution mechanisms of volatiles (e.g. H_2O, H_2, CO_2, CH_4,) in these phases is essential to constrain the melting and crystallization processes. Advances in our current understanding of stable isotope fractionations (e.g. $^{18}O/^{16}O$, $^{13}C/^{12}C$, D/H, $^{15}N/^{14}N$) under temperature and pressure conditions corresponding to lower crustal/-upper mantle conditions, and how this behavior can be related to structural roles of C-O-H-N-bearing volatiles in fluids and

melts have significant implications for the development of isotope proxies to describe the water cycle and to model elemental fluxes between different sources and sinks in the Earth's interior.

To investigate the role played by the condensed state on the isotope exchange reactions between deuterated and protionated molecules, Raman vibrational spectroscopy is an effective probe because of the large frequency separation of the D- and H- bearing functional groups [a factor of $1/\sqrt{2}$ (reduced mass effect)]. Accordingly, by combining Raman vibrational spectroscopy with experimental designs that allow *in-situ* monitoring of chemical processes at high temperatures and pressures (>600 ^{o}C, >300 MPa) (Bassett et al., 1996), D/H exchange between functional groups can be determined as a function of temperature and pressure. Thus, volume, enthalpy and entropy effects on isotopic distribution can be examined while the samples are at the desired temperature and pressure. For example, recent studies have shed light on the role of hydrogen bonding on the distribution of deuterated hydrogen dissolved in (D_2O+H_2O) aqueous solutions (Foustoukos and Mysen, 2012). These latter experiments were conducted at 300 – 800 ^{o}C and pressures between ~ 0.3 and 1.3 GPa and show significant deviation of the H_2-D_2-HD equilibrium relationship from the theoretical values predicted for gas phases (Bigeleisen and Mayer, 1947; Richet et al., 1977). There was also an apparent negative temperature effect possibly triggered by enthalpy contributions due to mixing of these species in supercritical water. This behavior has been attributed to differences in the strength of hydrogen bonding in the O-H···O relative to the O-D···O environment that could promote species solubility in dense and polar H_2O clusters. In turn, this affects the thermodynamic

properties of exchange reactions between the H/D hydrogen isotopologues and the coexisting H_2O-D_2O aqueous solutions.

Similar use of Raman spectroscopy can also be applied to study the D/H fractionation of (C-H)-bearing volatiles dissolved in supercritical fluids. For example, the multiple C-H bonds in methane allow for partial deuterium substitutions and result in the formation of deuterated isotopologues such as CH_3D, CH_2D_2, CHD_3, and CD_4. To the knowledge of the authors, only one theoretical study has been published to predict the equilibrium relationships between the different H/D isotopologues of methane and to model the stable hydrogen isotope fractionation of CH_4 with H_2O and H_2 over a range of temperatures (Bottinga, 1969). Experimental investigation of these isotopic molecules while a sample is at high temperature/-pressure, therefore, can provide ways to describe exchange reactions at conditions beyond those described in theoretical models. Such experiments lead to improved understanding of D/H fractionation effects in condensed matter (e.g. melts, fluids) at conditions relevant to the Earth's mantle.

Here, we examine the equilibrium relationships of the several H/D isotopologues of methane (i.e. CH_3D, CHD_3, CH_2D_2, CD_4) and evaluate the D/H molar ratios of methane developed under gas and condensed-phase (supercritical water) conditions, through a series of hydrothermal diamond anvil cell experiments conducted at 600 – 800 ^oC and 409 - 1622 MPa, while employing Raman vibrational spectroscopy as the analytical tool to trace reaction kinetics and pathways *in-situ* at elevated temperatures and pressures.

EXPERIMENTAL SECTION

Hydrothermal Diamond Anvil Cell. Experiments were performed with an externally-heated hydrothermal diamond anvil cell (HDAC) (Bassett et al., 1996). The cell was equipped with low-fluorescence 1-mm culet diamonds. Samples were hold between the anvil faces with a 125 μm thick rhenium gasket (500 μm diameter sample chamber). Prior to the actual experiments, a series of runs was conducted at 800 ^{o}C and 0.5 - 0.8 GPa with only H_2O in the cell to treat the gaskets hydrothermally. This procedure leads to the formation of a layer of inert Re oxide on the surface of the Re metal. Temperature was monitored and adjusted with chromel-alumel thermocouples in contact with the upper and lower diamonds. External heating was provided by Mo wire heaters placed around the tungsten carbide seats, and it was distributed homogeneously across and through the whole sample chamber (±1 ^{o}C accuracy). Pressure was derived by measuring the temperature/-pressure dependent Raman frequency shift of synthetic ^{13}C diamond (Schiferl et al., 1997), with an uncertainty of about ±40 MPa (Mysen and Yamashita, 2010). This level of accuracy is achieved by performing acquisitions at 2400 grooves/mm and then normalizing to the 584.72 nm Ne emission line; a protocol that yields a ± 0.1 cm^{-1} frequency uncertainty on the fundamental band of the ^{13}C diamond (Mysen and Yamashita, 2010).

Raman Spectroscopy Instrumentation. A Jasco model IRS-3100 confocal microRaman spectrometer was used with a λ_{ex} = 532 nm continuous wave laser line operating at ~7 mW at the sample. The beam diameter is nearly 1 μm. Signal detection was through 50X/0.42 numerical aperture (N.A.) and 10X/0.28 N.A. long-working distance

Mitutoyo™ objective lenses. Raman signal was dispersed using 1200 grooves/mm and with the spectral window centered at 1150 cm^{-1}, 2400 cm^{-1} and 3600 cm^{-1}; and collected with a Peltier-cooled CCD (Andor™ Model DV401-F1 1024x128 pixel with 25 μm pixel size) with a frequency resolution of 1-2 cm^{-1}. The system is equipped with a holographic notch filter. Acquisition time ranged from 150 (*in-situ* measurements) to 300 (quenched samples) sec/CCD window, and 2 acquisitions per window were collected.

Curve-fitting and background subtraction of the Raman spectra were orchestrated using the commercial software Igor from Wavemetrics™. Background subtraction was conducted prior to peak integration by fitting a third-order polynomial function through portions of the spectra with baseline signal intensity only. To constrain further the extent of uncertainty on spectra analysis and processing, replicate acquisitions (2-4) were performed at the same beam spot and with the same instrumental parameters. The standard deviation between the fitted Raman spectra reflects a 5% level of uncertainty, which is larger than the uncertainty estimated for the integrated area of each individual Raman peak. In the Raman spectra shown, the second-order Raman signal of the ^{12}C diamond anvils (~ 2300 - 2800 cm^{-1}) was removed by subtracting the background spectrum measured on the lower diamond and outside the sample gasket-chamber at the corresponding temperature and pressure.

Experimental Procedures. The experiments were designed to yield deuteromethane species through decomposition of $Si_5C_{12}H_{36}$ (tetrakis(trimethylsilyl) silane (Alfa Aesar 98% - natural D/H abundance) under both supercritical water and gas phase conditions. The study was carried out at temperatures of 600-800 ^oC and pressures of 409-1622 MPa.

149 The sample consisted of H_2O:D_2O (1:1 by volume) aqueous solutions with either metallic
150 Ni (Alfa Aesar, Puratronic 99.996%, <100 μm diameter grain) or metallic Pt (100 μm x
151 70μm OD rod) with no specific in-plane crystal orientation (e.g. Ni(111), Pt(111))
152 (Table 1) (Fig. 1). Complete decomposition of $Si_5C_{12}H_{36}$ resulting in the formation of
153 volatiles such as H_2, D_2, HD, CH_4, CH_3D, CHD_3, CH_2D_2 and CD_4 along with the
154 precipitation of quartz ($SiO_{2(s)}$), occurs within 5 min at 600 ^oC ($Si_5C_{12}H_{36}$ + $10H_2O/D_2O$
155 = $5SiO_2$ + $12CH_xD_y$ + $4H_xD_y$). In effect, decomposition of $Si_5C_{12}H_{36}$ with the use of
156 highly enriched in D_2O aqueous solutions allows for the synthesis of deuterated methane
157 species at abundances that permit quantification with spectroscopic methods. During this
158 initial, short stage of silane decomposition and deuterated isomers formation by methyl
159 radical reaction with the aqueous solution, kinetic isotope effects can be introduced.
160 However, time series measurements, *in-situ* at high temperature/-pressure, indicate that
161 chemical/isotopic equilibrium was reached within nearly 2 hours (at 600 and 800 ^oC) (see
162 more detail later in discussion), due to the enhanced kinetics of the exchange reactions
163 that proceed at the surface of either Ni or Pt (Beck et al., 2003; Horita, 1988; McKee and
164 Norton, 1964).

165 An important component of the experimental design is the abundance of starting
166 $Si_5C_{12}H_{36}$ relative to the volume of H_2O-D_2O solution encapsulated between the Re
167 gasket and the diamond culets. Two distinctly different sets of experiments ("gas phase"
168 and "liquid phase") were conducted by adjusting the silane/water proportions based on
169 volumetric approximations. For example, use of elevated silane/water initial ratios
170 resulted in the removal of H_2O through $SiO_{2(s)}$ precipitation at high temperature and the
171 establishment of gas phase conditions. When smaller amounts of silane were used, less

H/D-bearing methane species were produced and remained dissolved in the supercritical aqueous solution. These processes were documented by *in-situ* visual observation of the reaction progress (and the extent of quartz precipitation) (Fig. 1), and by monitoring the relative abundance of the coexisting fluid through the evolution of the O-H stretching band (~ 3600 cm^{-1}).

The Raman spectra of aqueous and gaseous species were recorded at the desired temperature/-pressure conditions and also in samples quenched to ambient conditions ("*ex-situ*"). Quenching was orchestrated at a rate of ~600 ^{o}C/min until the temperature reached 100 ^{o}C, and then at 25 ^{o}C /min to room temperature. During quenching and for the "liquid phase" experiments, phase separation (degassing) occurred leaving the H/D isotopologues of CH_4 and H_2 trapped in the gaseous phase ("bubble") (Fig. 2). The absence of the Raman lines assigned to the fundamental vibrational modes of HDO and D_2O at ~2400 – 2600 cm^{-1} (Foustoukos and Mysen, 2012; Walrafen et al., 1996) (revealed after subtracting the v_2 lines of diamond) is consistent with spectroscopic measurements on an *ex-situ* bubble. Slower rates of quenching (10 ^{o}C/min) were also applied to determine accurately the temperature and pressure of gas-liquid phase separation. At these conditions, the partial pressure of volatiles is equal to the confined pressure in the HDAC, and thus, total dissolved methane concentrations ($\Sigma CH_4 = CH_4 + CD_4 + CH_3D + CH_2D_2 + CHD_3$) (Table 1) can be retrieved from the solubility relationship: $\Sigma CH_{4(g)} \leftrightarrow \Sigma CH_{4(aq)}$. The equilibrium constant of this reaction is calculated at high temperature/-pressure by using the Helgeson-Kirkham-Flowers equation of state and the SUPCRT92 code that are applicable to 1000 ^{o}C and 500 MPa, effectively extrapolated to 1 GPa (Johnson et al., 1992b; Manning, 1998; Shock and Helgeson,

1990). The concentrations of the dissolved H/D hydrogen isotopologues appear to be minimal (but present) relative to methane (Fig. 2b) because of the relatively oxidizing redox conditions imposed by hydrothermal oxidation of Ni and Pt metals in H_2O-D_2O solutions. Manifestation of oxidizing conditions was also demonstrated by the formation of $CO_{2(aq)}$ and the precipitation of amorphous graphitic carbon at 800 ^oC (Table 1). Solution density is calculated following the PVT data of pure H_2O (Wagner and Pruss, 2002) applied to the homogenization conditions, while assuming minimal solubility for the crystalline phases (Ni, Pt, $SiO_{2(s)}$) (Johnson et al., 1992b; Robie and Hemingway, 1995).

RESULTS AND DISCUSSION

Spectroscopic data were collected mainly from the two frequency regions of 1560 – 3140 cm^{-1} and 2900 – 4220 cm^{-1} (1200 grooves/mm) where several vibration modes of the D- containing isotope molecules of CH_4 and H_2 are captured (Fig. 2). These species were identified both *in-situ* and in the quenched samples. The Raman spectra acquired from quenched bubbles allowed a detailed estimation of the relative abundances of the deuterated methane isotopologues (Fig. 2a). The bands assigned to stretch vibrations in these species are narrow (5-10 cm^{-1} FWHH) and well defined, relative to those registered during spectral acquisition at high-temperature/-pressure conditions.

The 2000 - 2400 cm^{-1} frequency envelope accommodates the bands of the asymmetric stretching and bending vibrations of the CHD_3 (2134 cm^{-1}, 2305 cm^{-1}), CH_3D - CH_2D_2 (~2190 cm^{-1}) and the C-D fundamental mode of the CD_4 molecule (2098 cm^{-1}) (Fig. 2a). However, because of the strong baseline correction introduced by subtracting

218 the complex group of bands assigned to the second-order vibration of the diamond anvils
219 (~ 2300-2800 cm^{-1}) from sample signal(s), the integrated peak areas of these bands have
220 large uncertainties. Their intensities cannot be used, therefore, to describe equilibrium
221 relationships between the isotopologues. For this purpose, we employ the fundamental
222 harmonics at the slightly higher frequencies of 2905 cm^{-1} (CH_4), 2961 cm^{-1} (CH_3D), 2966
223 cm^{-1} (CH_2D_2) and 2984 cm^{-1} (CHD_3). Vibrational assignments are in agreement with the
224 values reported in the experimental study of Kagel (1964) (1964) and the review article
225 of Schötter and Klöckner (1979) (1979) at room-temperature conditions, and internally
226 consistent with the correlation between peak intensities and the Raman scattering cross
227 sections for the different vibrational modes of the molecules of interest (Table 2) (Kagel,
228 1964; Schrotter and Klockner, 1979). Within the same spectral window, the fundamental
229 vibrations of C_2H_6 and C_3H_8 also reside. These carbon-bearing species could possibly be
230 formed by polymerization of the methyl radicals at high temperature (Spanu et al., 2011).
231 However, in preliminary experiments involving $Si_5C_{12}H_{36}$ decomposition in H_2O solution
232 at 600 ^oC, we did not observe their symmetric C-H and C-C vibrational bands at 2950-
233 2990 cm^{-1} and 870-995 cm^{-1}, respectively (Atamas et al., 2004; Shimanouchi, 1972),
234 concluding, therefore, that long chain hydrocarbons (< 100 μmolal (Foustoukos, 2010))
235 were undetectable in our experimental setup.

236 From the overall intensity relationships, the distribution of the deuteromethanes
237 suggests that deuterium enrichment was enhanced when dissolved in supercritical water
238 than when present as gas phase components (Fig. 2a). This could be attributed to the D/H
239 fractionation between methane and the coexisting H_2 or H_2O, however, the former is
240 highly improbable due to the significantly lower concentrations of hydrogen relative to

241 methane (Fig. 2b). Another hypothesis involves the introduction of kinetic isotopic
242 effects during high temperature/-pressure quenching and the subsequent phase
243 segregation of volatiles from the supercritical fluid (liquid-phase experiments). To assess
244 the contribution from such processes, a series of Pt- supercritical water- bearing
245 experiments were quenched to room temperature after being equilibrated at 600 ^{o}C –
246 1093 MPa and 800 ^{o}C – 1050 MPa for 480 and 540 minutes, respectively. The samples
247 were then immediately exposed to a second heating cycle that lasted for two hours. The
248 second series of temperature-quenching was at 55 ^{o}C /min as compared with the initial of
249 600 ^{o}C/min. Comparison between the Raman spectra of the quenched bubbles from two
250 individual liquid-phase bearing HDAC experiments that underwent two heating cycles
251 reveals no differences on the relative distribution of CH_xD_y species (Fig. 3). There is,
252 therefore, no evidence for retrograde reactions and kinetic isotope effects associated with
253 phase segregation during quenching of the high temperature/-pressure chemical
254 equilibrium to room temperature conditions.
255
256 **Distribution of deuterated methane isotopologues**
257 **Ex-situ Samples:** The spectral region between ~2800 – 3100 cm^{-1} that includes the
258 fundamental frequencies of CH_4, CH_3D, CH_2D_2 and CHD_3 (Fig. 4), allows for a detailed
259 examination of the equilibrium relationships between the isotopologues. In spectra of the
260 quenched bubbles, for example, there are well-defined peaks that can be de-convoluted
261 following Lorentzian (CH_4, CH_3D) and Gaussian (CH_2D_2) functions. Peak integration for
262 the tri-deuterated methane was carried out with both Gaussian and Lorentzian peak
263 shapes. Thus, subsequent comparison between the integrated intensities of the v_1-CH_xD_y

264 includes the average values of the v_1-CHD_3 peak area following these two fitting
265 distributions. Attempts to introduce the stretching vibrational mode of D_2 in the
266 frequency spectrum of the v_1-CHD_3 (~2970-2985 cm^{-1}) failed, largely because the v_1-D_2
267 intensity is inferred to be very small due to the low abundance of H_2 and HD (Fig. 2)
268 combined with the small Raman scattering cross section of the D_2 relative to the other
269 hydrogen species (Bischel and Black, 1983; Polavarapu, 1990; Schrotter and Klockner,
270 1979).

271 The distribution of the H/D methane isotopologues calculated from the integrated
272 peak areas follows a general abundance order of CH_4>CH_3D>CH_2D_2>CHD_3. This trend
273 is consistent with other experimental results of Pt-supported H-D exchange reaction
274 between methane and deuterium at elevated temperatures (McKee and Norton, 1964),
275 and also is in accord with the overall kinetic isotope effect expected from the higher
276 activation energy required for C-D bond formation relative to the C-H bond (Anslyn and
277 Dougherty, 2006).

278

279 **In-situ Samples:** For the spectra collected at high temperature/-pressure conditions, the
280 rapid broadening of the Raman lines and the decrease of spectral resolution with
281 increasing temperature (due to black body radiation) resulted in an extensive overlapping
282 and interference between the isotopologues. Black body radiation is transmitted from the
283 furnace and sample when at temperature higher than 600 ^oC, causing signal deterioration
284 and an increase of the background intensity. In addition, an overall decrease on the
285 intensities of the CH_xD_y (i.e. deuteromethanes) vibrations is expected when species are
286 dissolved in the supercritical H_2O-D_2O fluid.

To this end, peak de-convolution was performed by fitting Lorentzian curves assigned to the symmetric C-H stretching vibration of methane and to the frequency envelope that encloses the stretching vibrations of the other CH_xD_y species (Fig. 4). These *in-situ* measurements permit monitoring of reaction progress towards establishing chemical/isotopic equilibrium in the H_2O-D_2O-CH_4 system, while providing information regarding the condensed-phase isotope effects associated with the solvation of the H/D isotopologues in supercritical aqueous solutions.

To probe isotopic fractionations at experimental conditions, we employed the ratio between the integrated intensities of the Raman bands assigned to the H/D-isotopologue frequency envelope (v_1-CH_xD_y) and the C-H stretching of non-deuterated methane (v_1-CH_4) as a function of time (Fig. 5). From these results, we conclude that chemical/isotopic equilibrium was achieved within 2 hours, largely induced by the catalytic activities of Ni and Pt, which are enhanced at elevated surface thermal energy (Harris et al., 1991; Lutz and Bethune, 1989). There are also abundant concentrations of deuterated species in the liquid-phase system with the retrieved CH_xD_y/CH_4 intensity area ratios being nearly twice that in the gas-bearing system. Furthermore, platinum is shown to more efficiently promote the H/D exchange between C-H and C-D bonds than Ni. This observation is in agreement with previously published experimental and theoretical studies that support the greater probability of hydrogen/deuterium atoms to exchange when methyl groups bind on the Pt surface relative to when chemisorption occurs on Ni substrate (McKee and Norton, 1964; Nave et al., 2010). Experimental methodologies adopted, however, cannot provide further information regarding the CH_3- dissociative absorption on catalyst's surface nor the mechanism of isotope exchange reactions/-

diffusion (Wonchoba and Truhlar, 1996) associated with H and D atoms embedded in the metal lattice (Johnson et al., 1992a; Killelea et al., 2008; Wonchoba and Truhlar, 1998).

Condensed Phase Isotope Effects

Results indicative of increased deuteration of methane when dissolved in supercritical water were also obtained from interpreting Raman vibrational spectra collected *ex-situ* at 25 ^{o}C (Fig. 6a). This was accomplished by combining the integrated peak areas (Fig. 4) with the well-constrained relative normalized differential Raman scattering cross sections (σ_j) of the stretch vibrations (Table 2). Species concentrations are then considered proportional to the quotient of the integrated Raman peak areas (A_j) with (σ_j) assuming that the force constants are the same for the fundamental vibrational modes of CH_xD_y when instrumental parameters are constant (Kagel, 1964). Accordingly, the D/H molar composition of methane can be defined as such:

$$D/H = \frac{\sum_{n=1}^{3} \frac{A_j}{\sigma_j} CH_{4-n}D_n + \frac{A_{CD_4}}{\sigma_{CD_4}}}{A_{CH_4}/\sigma_{CH_4}} \quad (1)$$

Integrated area contributions from the Lorentzian peak shape of v_1-CD_4 (2098 cm^{-1}) are included because D/H molar ratios estimated with or without this factor exhibit the same mean values and range of uncertainties.

Experimental results demonstrate that the D/H molar composition of methane is increased by a factor of 2 in the liquid-bearing experiments compared with the gas-bearing system (Fig. 6a) (Table 3). Obvious also is the effectiveness of Pt over Ni as catalyst for the reconstruction of the C-H and C-D bonds, and for possible tunneling of hydrogen during chemisorption of methyl radical on hot metal surfaces (Harris et al.,

1991). Thermal vibrational energy provided by excitation of the fundamental stretch of the C-H/D bonds could also promote the reaction between H- and deuterated methyl radicals through bond cleavage (Beck et al., 2003; Crim, 2008). However, a decrease in activation barriers with increasing temperature of coexisting compounds (methane, metal) is expected to drive the process (Lutz and Bethune, 1989), especially for the low-power laser beam (7 mW) deployed. The effect of externally imposed thermal energy on D/H exchange reactions can also be inferred from the slight increase of the methane D/H molar ratios when shifting thermal conditions from 600 to 800 ^{o}C (Fig. 6a).

Kinetic isotope effects associated with hydrogen isotope fractionation between methane and water fluid could also explain the higher D/H ratio of the methane when dissolved in supercritical D_2O-H_2O aqueous solutions compared with the D/H ratio of the methane in the gas phase system. In addition, kinetic isotope effects can be introduced by the reforming of deuterated isomers on the catalyst surface. To evaluate such possible effects, the equilibrium relationship between the methane isotopologues was studied through the following reaction:

$$CH_3D + CH_2D_2 \rightarrow CHD_3 + CH_4 \quad (2)$$

By utilizing the vibrational characteristics of the different species (i.e. A_j and σ_j) and by assuming that the activity of neutral species is equal to their concentration under homogeneous gas phase conditions and for a non-electrolyte mixture of H_2O-D_2O, the equilibrium constant of this reaction is expressed as:

$$K_{eq}(CH_xD_y - CH_4) = \frac{A_{CH_4} * A_{CHD_3}}{A_{CH_3D} * A_{CH_2D_2}} * \frac{\sigma_{CH_3D} * \sigma_{CH_2D_2}}{\sigma_{CH_4} * \sigma_{CHD_3}} \quad (3)$$

For the C-H-D system in supercritical H_2O+D_2O at 873-1073 K (Fig. 6b), estimated K_{eq} values range from 0.42 ± 0.07 (Ni) to 0.59 ± 0.12 (Pt), corresponding to ΔG_{rxn} of 7.1 ±

355 1.4 and 4.3 ± 1.7 kJ/mol, respectively (Table 3). Differences on the estimated K_{eq} are
356 within analytical uncertainties, and likely reflect the greater efficiency of Pt over Ni in
357 promoting D/H isotope exchange reactions (Beck et al., 2003; Horita, 1988; McKee and
358 Norton, 1964; Nave et al., 2010). This observation does not preclude the establishment of
359 equilibrium conditions supported by the *in-situ* time series measurements conducted at
360 the course of the Pt-bearing experiments (Fig. 4). It also appears to be an exothermic
361 reaction, however, the possible temperature dependence of the equilibrium constant may
362 be somewhat obscured by the analytical errors introduced after adopting the combination
363 of Lorentzian and Gaussian functions (Fig. 4) and the vigorous analytical/peak
364 integration protocols discussed earlier.

365 When these values are compared to those derived for the gas-bearing system, the
366 role of supercritical water in affecting the equilibrium between H/D methane
367 isotopologues is evident (Fig. 6b). In effect, K_{eq} is shifted to 0.27 ± 0.04, reflecting a
368 ΔG_{rxn} of 10.7 ± 1.1 kJ/mol and minimal differences between the Ni- and Pt- catalyzed
369 experiments. Interestingly, these values are in close agreement with theoretical
370 calculations (K_{eq} = 0.16) conducted following standard state canonical partition functions
371 and conditions of ideal gas mixing (Bottinga, 1969); a conclusion that furthers supports
372 the establishment of chemical/isotopic equilibrium in these experiments. Most
373 importantly, the different thermodynamic properties of the equilibrium relationship
374 between H/D methane isotopologues attained for the gas- and liquid- phase system, allow
375 us to decouple possible kinetic isotope effects linked to the D/H fractionation between
376 CH_4 and H_2O with the extensive deuteration of methane observed in the liquid-bearing

377 experiments, and thus, focus on solvation effects in the condensed supercritical-fluid
378 phase.

379 Considering all of the above, the differences on the extent of D/H exchange and
380 the H/D isotopologues' distribution between the gas- and supercritical-fluid bearing
381 systems are attributed to condensed-phase isotope effects. Such processes can involve
382 changes in solubility induced by differences in Henry's law constants of the deuterium-
383 substituted isotopologues reflecting different standard-state free energies of solvation for
384 infinite dilution in the H_2O-D_2O cage (Bacsik et al., 2002; Chamberlin et al., 2006;
385 Gomes and Grolier, 2001). These effects are, in general, introduced when excess Gibbs
386 free energy of mixing is developed due to the presence of intermolecular interactions
387 between C-H-D species and the hydrogen bonded to H_2O/D_2O molecules (Jancso et al.,
388 1993; Van Hook, 2006). Here, differences in the strength of the O-D···D and O-H···H
389 bonds can influence the solvent properties of the D_2O-H_2O mixtures. In essence, titration
390 of H_2O-D_2O solutions and the formation of HDO through the endothermic reaction
391 between H_2O-D_2O has been proposed to rearrange the H and D bonding environment
392 (Graziano, 2000; Katsir et al., 2010), resulting in excess entropy costs for the solvation of
393 non-polar molecules in D_2O-H_2O. Furthermore, evidence exists for a temperature
394 dependent distribution of O-D···D and O-H···H bonds in supercritical fluids driven by the
395 increasingly stronger hydrogen bonding in H_2O relative to D_2O with temperature increase
396 (Erickson et al., 2011; Foustoukos and Mysen, 2012). Accordingly, contributions from
397 isotope effects governed by the solvent because of the employment of D_2O-enriched
398 aqueous solutions cannot be excluded.
399

D/H FRACTIONATIONS IN THE EARTH'S INTERIOR

Experimental results presented support extensive hydrogen isotope fractionation at high temperatures/-pressures when methane is dissolved in the condensed supercritical water phase relative to systems adopting ideal gas behavior. At such thermal conditions statistical thermodynamic models predict small isotope effects following vibrational zero point energy distributions and high temperature anharmonicity contributions for isotopic molecules in ideal-gas reference state (Bottinga, 1969). These models, however, do not account for solubility and solvent isotope effects associated with the solvation of H/D methane isotopologues in supercritical aqueous solutions and/or silicate melts. The theory of condensed-phase isotope effect follows the same Born-Oppenheimer approximation as the canonical approach for calculating the potential energy surface of the isotopic molecules, but also includes inputs from intermolecular forces developed in the condensed phase to the shape and the kinetic energy of the potential energy surface (Van Hook, 2006). In our study, the *in-situ* and *ex-situ* spectroscopic measurements of deuterated methane species coexisting with supercritical water suggest a significant contribution from condensed-phase isotope effects, rendering essential any further theoretical studies to assess the atomistic details of the D/H fractionation mechanisms in aqueous solutions (and silicate melts) at elevated temperature/-pressure conditions.

Condensed-phase isotope effects are expected to play a significant role on the distribution of deuterium and hydrogen species between C-O-H-N-saturated melts and coexisting fluids (Mysen, 2012), since this distribution can be affected by the abundance ratios of the different C, N and H-bearing structural complexes in the equilibrated phases (Hirschmann et al., 2012; Mysen and Fogel, 2010; Mysen et al., 2009). These structural

423 complexes in melt formed upon solution of H-bearing species likely contribute to the
424 D/H budget of the mantle and the isotopic composition of evolved magmatic fluids
425 (Kasting et al., 1993; Mattey et al., 1990).

426 For example, isotope fractionation effects between phases coexisting in Earth's
427 interior likely constrain the observed D/H disequilibrium between mantle and oceanic
428 H_2O reservoir, as well as the subduction zone contributions to the mantle-water cycle
429 (Hauri, 2002; Shaw et al., 2008) (and references therein). The disequilibrium
430 relationships between water reservoirs imply that cycling of water in the mantle is not
431 extensive and/or hydrogen isotope fractionation effects are imposed between the oceanic
432 water and the amorphous/crystalline phases of the Earth's interior (Shaw et al., 2008).

433 Magmatic degassing of C-O-H-N volatiles during magma ascent and the
434 subsolidus dehydration of hydrous minerals are also expected to induce hydrogen
435 fractionation effects between fluids and mineral phases (Suzuoki and Epstein, 1976;
436 Taylor et al., 1983). Molecular water appears to concentrate deuterium relative to silicate
437 melts/minerals, while the dehydration of OH from minerals likely yields to a decrease in
438 both D and water content (Suzuoki and Epstein, 1976). Degassing of CH_4 and H_2 from a
439 magma that contains small amounts of H_2O can also result in significant changes in the
440 δD of melt (Kyser and Oneil, 1984), driven by the possible large D/H fractionation
441 factors between CH_4 and H_2 with H_2O at high temperatures. Accordingly, further studies
442 are needed to constrain the fundamental mechanisms of stable isotope fractionation
443 between C-O-H-N species and functional groups dissolved in phases and at conditions
444 resembling those of the Earth's interior.
445

ACKNOWLEDGMENTS

This research was conducted with support from the Carnegie Institution of Washington (DF), the NSF-OCE-0928443 (DF), the NSF-EAR-0734182 (BM), the NSF-EAR-1250499 (DF, BM) and a NASA Astrobiology Institute (BM). A grant from the W. M. Keck Foundation supported acquisition of the Jasco IRS-3100 microRaman and the Jasco IMV4000 microFTIR spectrometers. Li Zhang synthesized the ^{13}C diamond, and her efforts are greatly appreciated.

454

Table 1. Description of the H_2O-D_2O-methane bearing HDAC experiments

T (K)	P (MPa)	Reaction Time (min)	T_h[a] (^oC)	P_h[a] (MPa)	$\Sigma CH_{4(aq)}$ (M)	Catalyst	Oxidized C
			Gas phase experiments				
873	577 ± 2	320				Ni	
1073	758 ± 99	204				Ni	Graphite[b]
873	514 ± 18	510				Pt	
1073	1105 ± 182	410				Pt	CO_2[c]
			Liquid phase experiments				
873	409 ± 26	435	342	314	1.73	Ni	
1073	1622 ± 131	545		*fluid density 0.6 g/cm^3*			CO_2
873	1093 ± 157	480	350	774	0.27	Pt	
1073	1050 ± 157	540		*fluid density 0.57 g/cm^3*			CO_2

[a] Temperature and pressure of the gas-liquid phase homogenization/separation. At these conditions, dissolved volatile species separate from the supercritical fluid forming a gas phase. [b] Precipitation of amorphous graphitic carbon was documented in the retrieved solid reaction products by the strong presence of the D (~ 1325 cm^{-1}) and G (~ 1570 cm^{-1}) bands accompanied by their second-order overtone and combination scattering at 2670 cm^{-1} (S_1) and 2910 cm^{-1} (S_2). [c] Spectroscopic evidence for the formation of CO_2 in both the high temperature/-pressure and quenched samples is the presence of frequency splitting of the v_1:$2v_2^0$ Fermi diad at 1275 cm^{-1} and 1378 cm^{-1}.

455

Table 2. Relative normalized differential Raman scattering cross sections of the fundamental vibrational frequencies of D-H isotopologues normalized to the value of the CH_4 molecule (25 ^oC)

	σ_j (σ_{CH4} =1)	Ref.
CH_3D	0.75	Schrötter and Klöckner (1979), Bermejo et al. (1977)
CH_2D_2	0.55	
CHD_3	0.33	
CD_4	0.73	
CH_3D	0.78	Kagel (1964)
CH_2D_2	0.52	
CHD_3	0.36	
CD_4	0.71	

456

457

458

Table 3. Thermodynamic properties estimated for the CH_3D + CH_2D_2 → CHD_3 + CH_4 reaction from *ex-situ* measurements

T (^oC)	P (MPa)	Metal	K_{eq}	ΔG_r (kJ/mol)
		Gas phase experiments		
600	577 ± 2	Ni	0.31 ± 0.05	8.6 ± 1.2
800	758 ± 99	Ni	0.26 ± 0.02	12.2 ± 0.7
average			*0.28 ± 0.04*	*10.4 ± 1.0*
600	514 ± 18	Pt	0.27 ± 0.04	9.5 ± 1.2
800	1105 ± 182	Pt	0.25 ± 0.04	12.5 ± 1.3
average			*0.26 ± 0.04*	*11.0 ± 1.2*
		Liquid phase experiments		
600	409 ± 26	Ni	0.43 ± 0.08	6.1 ± 1.4
800	1622 ± 131	Ni	0.40 ± 0.06	8.2 ± 1.4
average			*0.42 ± 0.07*	*7.1 ± 1.4*
600	1093 ± 157	Pt	0.60 ± 0.11	3.7 ± 1.3
800	1050 ± 157	Pt	0.58 ± 0.13	4.9 ± 2.0
average			*0.59 ± 0.12*	*4.3 ± 1.7*

459

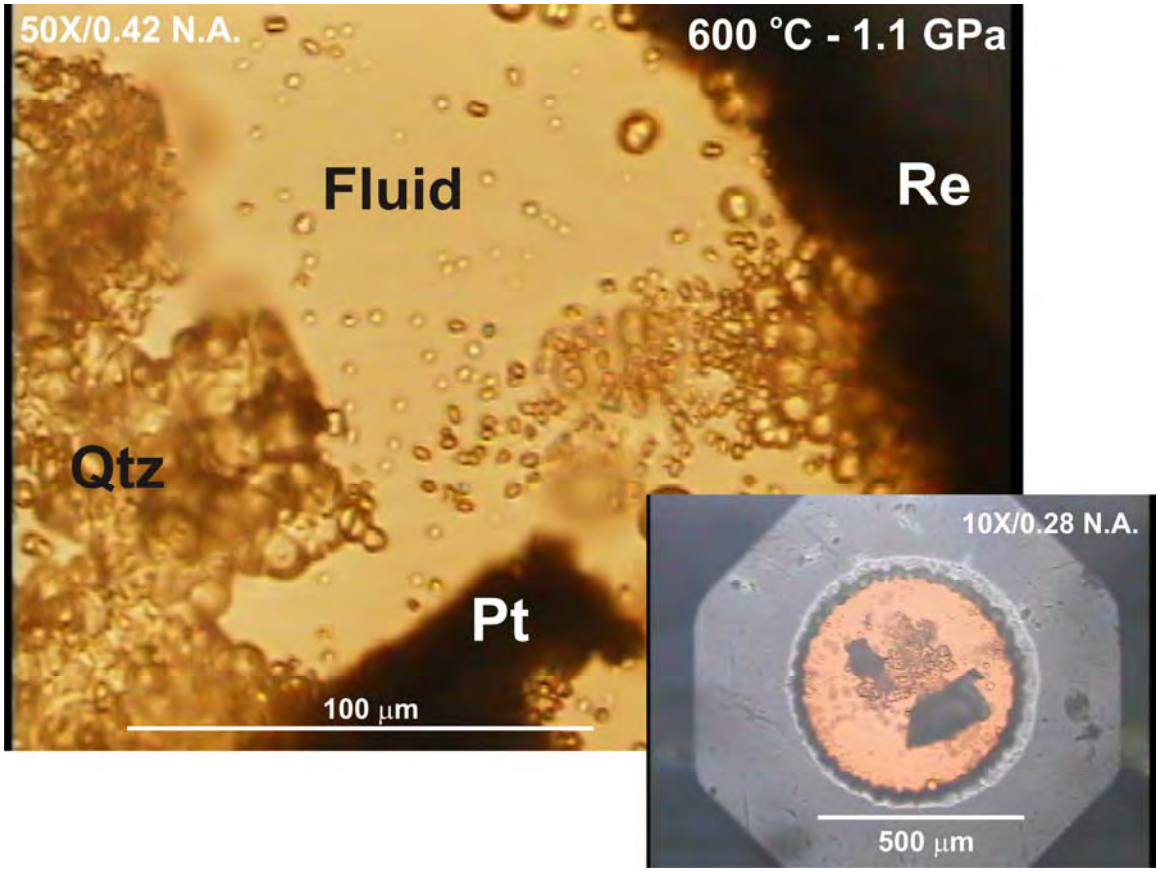

460

461

462 **Figure 1.** Microphotographs depicting phases involved in the high temperature/-pressure
463 HDAC experiments. Hydrothermal decomposition of $Si_5C_{12}H_{36}$ in D_2O-H_2O aqueous
464 solution and in the presence of metal catalyst (Ni, Pt) resulted to the formation of H/D
465 methane isotopologues, and the precipitation of $SiO_{2(s)}$.

466

467

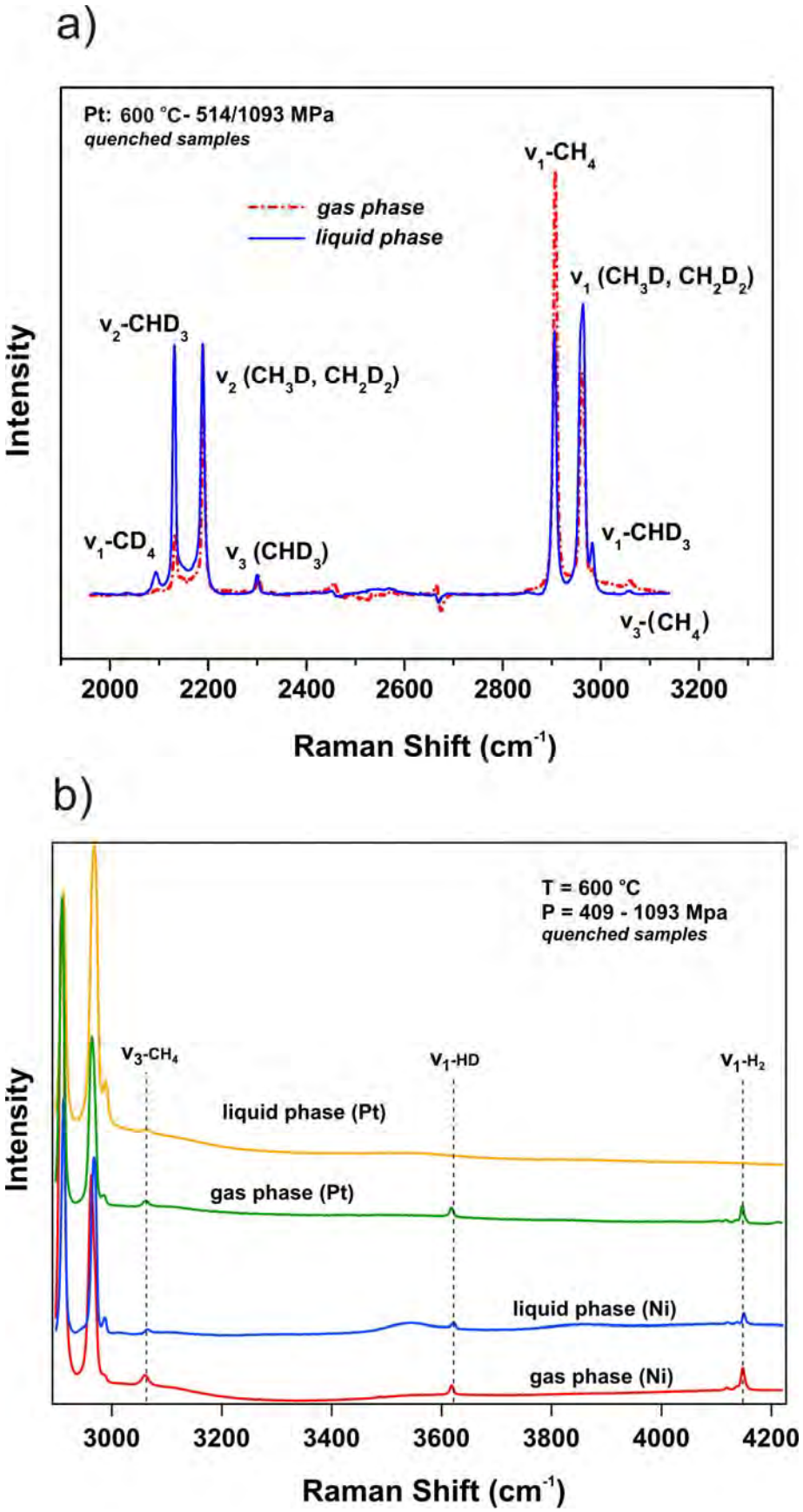

468

469
470 **Figure 2**. Examples of Raman spectra collected in samples quenched from high
471 temperature/-pressure conditions. Degassing processes induced during quenching allow
472 the formation of gas bubbles that contain H/D isotopologues of methane (a) and hydrogen
473 (b).
474
475

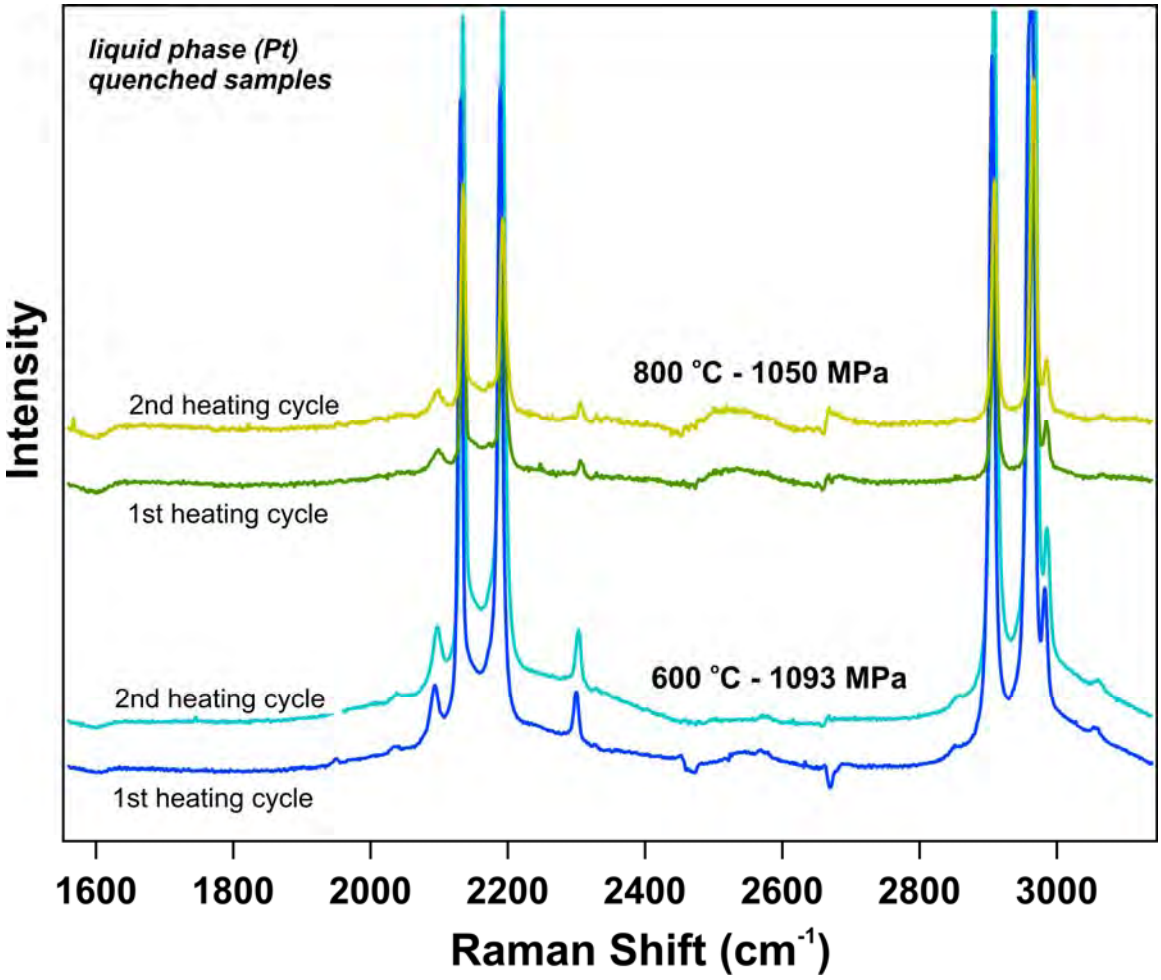

476

477 **Figure 3.** Vibrational spectra collected in samples from two district liquid-phase (Pt)
478 HDAC experiments at 600 ^{o}C and 800 ^{o}C that were subjected to two heating cycles and
479 then quenched at two different rates. Peak assignments are comparable to those shown in
480 figure 2a.

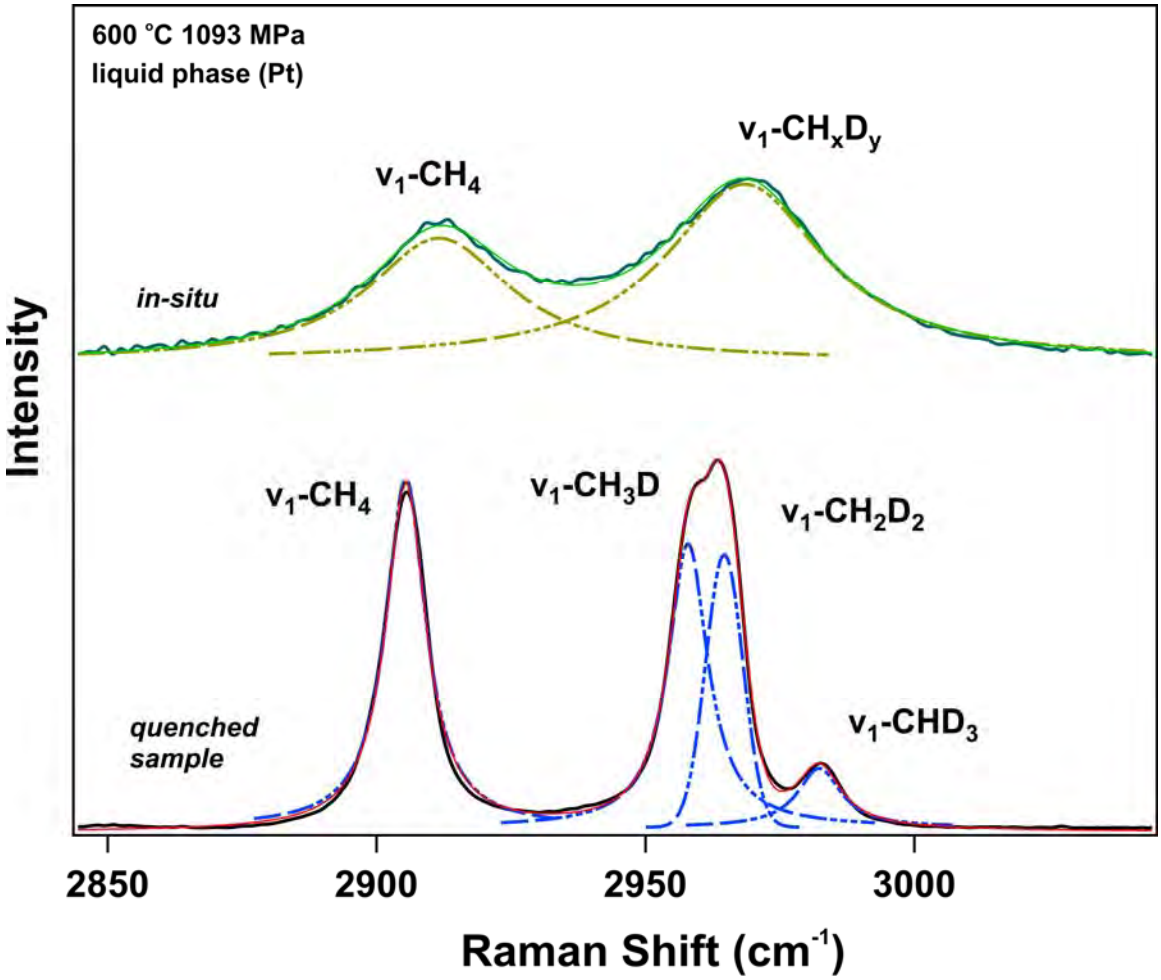

Figure 4. Examples of curved-fitted Raman spectra recorded within the 2800 – 3100 cm^{-1} frequency region that encompasses the fundamental frequencies of CH_4, CH_3D, CH_2D_2 and CHD_3.

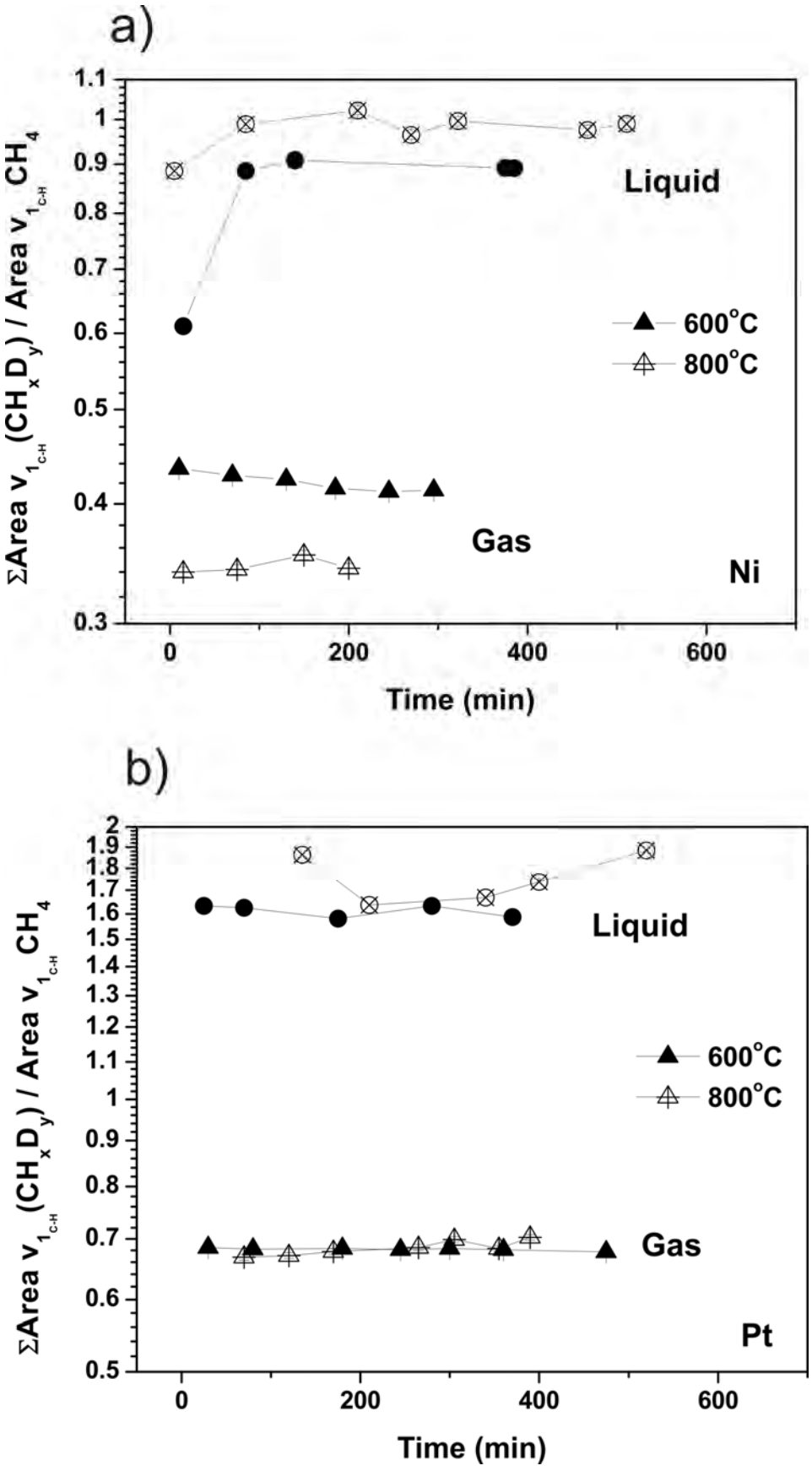

486

487 **Figure 5.** Times series measurements conducted *in-situ* at high temperature/-pressure and
488 in the presence of either Ni (a) or Pt (b) metal catalyst to describe the evolution of the
489 ratio between the integrated peak areas of the frequency envelope that encompasses the
490 v_1-CH_xD_y and the stretching vibrational mode of CH_4.
491

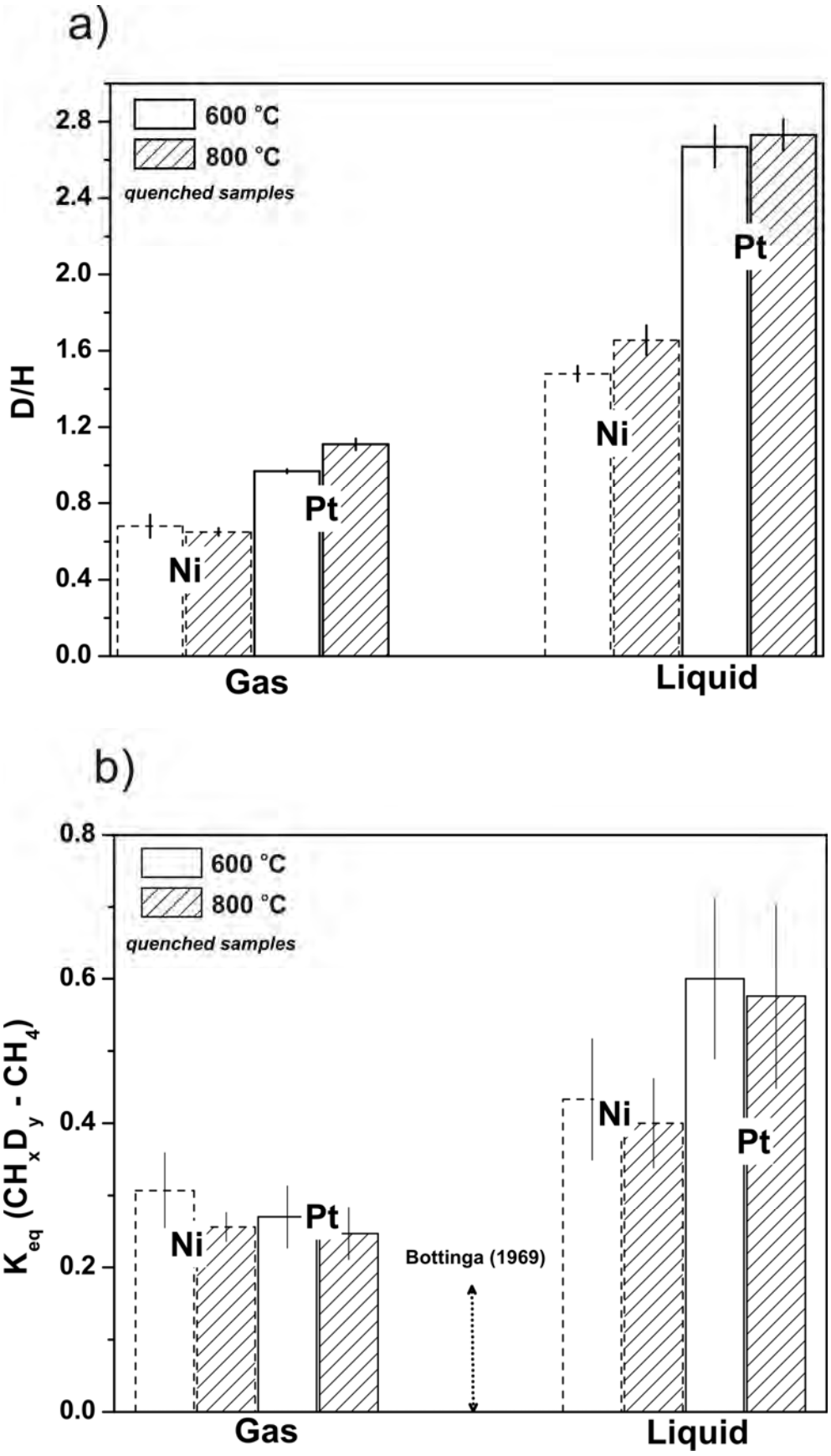

492

493 **Figure 6.** (a) The D/H molar ratios of methane measured in quenched samples as
494 function of the temperature, the metal catalyst and the phases present. Uncertainties
495 shown reflect the standard deviation between ratios estimated with/without contributions
496 from the v_1-CD_4 (b) The relationship between isotopologues is examined through the
497 equilibrium constant of the reaction: $CH_3D + CH_2D_2 \rightarrow CHD_3 + CH_4$. Experimental data
498 are compared to statistical models developed for ideal-gas reference state (Bottinga,
499 1969). Estimated errors correspond to the different integrated peak areas calculated
500 through a combination of Lorentzian and Gaussian functions for the de-convolution of
501 the CH_xD_y frequency envelope at 2900 - 2990 cm^{-1}.
502
503

REFERENCES SITED

Anslyn, E.V., and Dougherty, D.A. (2006) Modern physical organic chemistry. xxviii, 1095 p. p. University Science, Sausalito, CA.

Atamas, N.A., Yaremko, A.M., Seeger, T., Leipertz, A., Bienko, A., Latajka, Z., Ratajczak, H., and Barnes, A.J. (2004) A study of Raman spectra of alkanes in the Fermi-resonance region. Journal of Molecular Structure, 708, 189-195.

Bacsik, Z., Lopes, J.N.C., Gomes, M.F.C., Jancso, G., Mink, J., and Padua, A.A.H. (2002) Solubility isotope effects in aqueous solutions of methane. The Journal of Chemical Physics, 116(24), 10816-10824.

Bassett, W.A., Wu, T.C., Chou, I.M., Haselton, H.T., Jr., , Frantz, J., Mysen, B.O., Huang, W.L., Sharma, K., and Schiferl, D. (1996) The hydrothermal diamond anvil cell (HDAC) and its applications. In M.D. Dyar, McCammon C., and W.M. Schaefe, Eds. Mineral Spectroscopy: A Tribute to Roger G. Burns. The Geochemical Society Special Publication, No. 5, p. 261-272.

Beck, R.D., Manori, P., Papageorgopoulos, D., Dang, T.T., Schmid, M.P., and Rizzo, T.R. (2003) Vibrational mode-specific reaction of methane on a nickel surface. Science, 302, 98-100.

Bermejo, D., Escribano, R., and Orza, J.M. (1977) Absolute Raman intensities of CH_4, CH_3D, CH_2D_2, CHD_3, and CD_4. Journal of Molecular Spectroscopy, 65(3), 345-353.

Bigeleisen, J. (2006) Theoretical basis of isotope effects from an autobiographical perspective. In Ammon Kohen, and H.-H. Limbach, Eds. Isotope effects in chemistry and biology, p. 1-40. CRC Press, Boca Raton, FL.

Bigeleisen, J., and Mayer, M.G. (1947) Calculation of equilibrium constants for isotopic exchange reactions. The Journal of Chemical Physics, 15(5), 261-267.

Bischel, W.K., and Black, G. (1983) Wavelength dependence of Raman-scattering cross-sections from 200-600 Nm. Aip Conference Proceedings(100), 181-187.

Bottinga, Y. (1969) Calculated fractionation factors for carbon and hydrogen isotope exchange in system calcite-carbon dioxide-graphite-methane-hydrogen-water vapor. Geochimica et Cosmochimica Acta, 33(1), 49-64.

Chamberlin, A.C., Cramer, C.J., and Truhlar, D.G. (2006) Predicting aqueous free energies of solvation as functions of temperature. Journal of Physical Chemistry B, 110(11), 5665-5675.

Chialvo, A.A., and Horita, J. (2003) Isotopic effect on phase equilibria of atomic fluids and their mixtures: A direct comparison between molecular simulation and experiment. The Journal of Chemical Physics, 119(8), 4458-4467.

Crim, F.F. (2008) Chemical dynamics of vibrationally excited molecules: Controllong reactions in gases and on surfaces. Proceedings of the National Academy of Sciences of the United States of America, 105(35), 12654-12661.

Erickson, K.M., Arcis, H., Raffa, D., Zimmerman, G.H., and Tremaine, P.R. (2011) Deuterium isotope effects on the ionization constant of acetic acid in H_2O and D_2O by AC conductance from 368 to 548 K at 20 MPa. The Journal of Physical Chemistry B, 115, 3038-3051.

Foustoukos, D.I. (2010) Methane oxidation and formation of metastable organics under hydrothermal and supercritical water conditions. The 2nd Deep Carbon Cycle International Conference, Beijing, China.

Foustoukos, D.I., and Mysen, B.O. (2012) D/H isotopic fractionation in the H_2-H_2O system at supercritical water conditions: Composition and hydrogen bonding effects Geochimica et Cosmochimica Acta, 86, 88-102.

Gomes, M.F.C., and Grolier, J.P. (2001) Determination of Henry's law constants for aqueous solutions of tetradeuteriomethane between 285 and 325 K and calculation of the H/D isotope effect. Physical Chemistry Chemical Physics, 3(6), 1047-1052.

Graziano, G. (2000) On the solvent isotope effect in hydrophobic hydration. The Journal of Physical Chemistry B, 104, 9249-9254.

Harris, J., Simon, J., Luntz, A.C., Mullins, C.B., and Rettner, C.T. (1991) Thermally assisted tunneling: CH_4 dissociation on Pt(111). Physical Review Letters, 67(5), 652-655.

Hauri, E. (2002) SIMS analysis of volatiles in silicate glasses, 2: isotopes and abundances in Hawaiian melt inclusions. Chemical Geology, 183(1-4), 115-141.

Herzfeld, K.F., and Teller, E. (1938) The vapor pressure of isotopes. Physical Review, 54, 912-915.

Hirschmann, M.M., Withers, A.C., Ardia, P., and Foley, N.T. (2012) Solubility of molecular hydrogen in silicate melts and consequences for volatile evolution of terrestrial planets. Earth and Planetary Science Letters, 345, 38-48.

Horita, J. (1988) Hydrogen isotope analyses of natural waters using an H_2-water equilibration method: A special implication to brines. Chemical Geology, 72, 89-94.

Jancso, G., Rebelo, L.P.N., and Vanhook, W.A. (1993) Isotope Effects in Solution Thermodynamics - Excess Properties in Solutions of Isotopomers. Chemical Reviews, 93(8), 2645-2666.

Johnson, A.D., Daley, S.P., Utz, A.L., and Ceyer, T. (1992a) The chemistry of bulk hydrogen: Reaction of hydrogen embedded in nickel with adsorbed CH_3. Science, 257, 223-225.

Johnson, J.W., Oelkers, E.H., and Helgeson, H.C. (1992b) SUPCRT92 - A software package for calculating the standard molal thermodynamic properties of minerals, gases, aqueous species, and reactions from 1-bar to 5000-bar and 0°C to 1000°C. Computers and Geosciences, 18(7), 899-947.

Kagel, R.O. (1964) Vibrational Intensity Studies. University of Minnesota.

Kasting, J.F., Eggler, D.H., and Raeburn, S.P. (1993) Mantle Redox Evolution and the Oxidation-State of the Archean Atmosphere. Journal of Geology, 101(2), 245-257.

Katsir, Y., Shapira, Y., Mastai, Y., Dimova, R., and Ben-Jacob, E. (2010) Entropic effects and slow kinetics revealed in titrations of D_2O-H_2O solutions with different D/H ratios. The Journal of Physical Chemistry B, 114, 5755-5763.

Killelea, D.R., Campbell, V.L., Shuman, N.S., and Utz, A.L. (2008) Bond-selective control of a heterogeneously catalyzed reaction. Science, 319, 790-793.

Kirkwood, J.G. (1934) Quantum statistics of almost classical assemblies. Physical Review, 45(2), 0116-0117.

Kyser, T.K., and Oneil, J.R. (1984) Hydrogen isotope systematics of submarine basalts. Geochimica et Cosmochimica Acta, 48(10), 2123-2133.

Lutz, A.C., and Bethune, D.S. (1989) Activation of methane dissociation on a Pt(111) surface. The Journal of Chemical Physics, 90, 1274-1280.

Manning, C.E. (1998) Fluid composition at the blueschist - eclogite transition in the model system Na_2O-MgO-Al_2O_3-SiO_2-H_2O-HCl. Schweizerische Mineralogische und Petrographische Mitteilungen, 78(2), 225-242.

Mattey, D.P., Taylor, W.R., Green, D.H., and Pillinger, C.T. (1990) Carbon isotopic fractionation between CO_2 vapor, silicate and carbonate melts - an experimental study to 30 Kbar. Contributions to Mineralogy and Petrology, 104(4), 492-505.

McKee, D.W., and Norton, F.J. (1964) Catalytic exchange of methane and deuterium on platinum, ruthenium and platinum-ruthenium alloys. The Journal of Physical Chemistry, 68(9), 481-489.

Muccitelli, J., and Wen, W.Y. (1978) Solubilities of hydrogen and deuterium gases in water and their isotope fractionation factor. Journal of Solution Chemistry, 7(4), 257-267.

Mysen, B.O. (2012) Hydrogen isotope fractionation between coexisting hydrous melt and silicate-saturated aqueous fluid: An experimental study in-situ at high pressure and temperature. American Mineralogist, in press.

Mysen, B.O., and Fogel, M.L. (2010) Nitrogen and hydrogen isotope compositions and solubility in silicate melts in equilibrium with reduced (N plus H)-bearing fluids at high pressure and temperature: Effects of melt structure. American Mineralogist, 95(7), 987-999.

Mysen, B.O., Fogel, M.L., Morrill, P.L., and Cody, G.D. (2009) Solution behavior of reduced C-O-H volatiles in silicate melts at high pressure and temperature. Geochimica et Cosmochimica Acta, 73(6), 1696-1710.

Mysen, B.O., and Yamashita, S. (2010) Speciation and solubility of reduced C-O-H fluids in coexisting fluids and silicate melts determined in situ to 1.45 GPa and 800^{o}C. Geochimica et Cosmochimica Acta, 74, 4577-4588.

Nave, S., Tiwari, K.A., and Jackson, B. (2010) Methane dissociation and adsoprtion on Ni(111), Pt(111), Ni(100), Pt(100) and Pt(100)-(1x2): Energetic study. The Journal of Chemical Physics, 132, 054705.

Polavarapu, P.L. (1990) Ab initio vibrational Raman and Raman optical activity spectra. The Journal of Physical Chemistry, 94(21), 8106-8112.

Richet, P., Bottinga, Y., and Javoy, M. (1977) A review of hydrogen, carbon, nitrogen, oxygen, sulphur, and chlorine stable isotope fractionation among gaseous molecules. Annual Review of Earth and Planetary Sciences, 5, 65-110.

Robie, R.A., and Hemingway, B.S. (1995) Thermodynamic properties of minerals and related substances at 298.15K and 1 bar (10^5 pascals) pressure and at higher temperatures. U.S. Geol. Survey Bull., 2131, 462.

Schiferl, D., Nicol, M., Zaug, J.M., Sharma, S.K., Cooney, T.F., Wang, S.-Y., Anthony, T.R., and Fleischer, J.F. (1997) The diamond $^{13}C/^{12}C$ isotope Raman pressure sensor system for high temperature/pressure diamond-anvil cells with reactive samples. Journal of Applied Physics, 82, 3256-3265.

636 Schrotter, H.W., and Klockner, H.W. (1979) Raman scattering cross sections in gases and
637 liquids. In A. Weber, Ed. Raman spectroscopy of gases and liquids. Springer-
638 Verlag, New York.
639 Shaw, A.M., Hauri, E.H., Fischer, T.P., Hilton, D.R., and Kelley, K.A. (2008) Hydrogen
640 isotopes in Mariana arc melt inclusions: Implications for subduction dehydration
641 and the deep-Earth water cycle. Earth and Planetary Science Letters, 275(1-2),
642 138-145.
643 Shimanouchi, T. (1972) Tables of molecular vibrational frequencies consolidated volume
644 I. National Bureau of Standards, 1-160.
645 Shock, E., L, and Helgeson, H.C. (1990) Calculation of the thermodynamic and transport
646 properties of aqueous species at high pressures and temperatures: Standard partial
647 molal properties of organic species. Geochimica et Cosmochimica Acta, 54, 915-
648 945.
649 Spanu, L., Donadio, D., Hohl, D., Schwegler, E., and Galli, G. (2011) Stability of
650 hydrocarbons at deep Earth pressures and temperatures. Proceedings of the
651 National Academy of Sciences of the United States of America, 108(17), 6843-
652 6846.
653 Suzuoki, T., and Epstein, S. (1976) Hydrogen isotope fractionation between OH-bearing
654 minerals and water. Geochimica et Cosmochimica Acta, 40(10), 1229-1240.
655 Taylor, B.E., Eichelberger, J.C., and Westrich, H.R. (1983) Hydrogen isotopic evidence
656 of rhyolitic magma degassing during shallow intrusion and eruption. Nature, 306,
657 541-545.
658 Van Hook, W.A. (2006) Condensed matter isotope effects. In A.K.a.H.-H. Limbach, Ed.
659 Isotope effects in chemistry and biology, p. 119-152. CRC Press, Boca Raton, FL.
660 Wagner, W., and Pruss, A. (2002) The IAPWS formulation 1995 for the thermodynamic
661 properties of ordinary water substance for general scientific use. Journal of
662 Physical and Chemical Reference Data, 31(387-535).
663 Walrafen, G.E., Yang, W.H., Chu, Y.C., and Hokmabadi, M.S. (1996) Raman OD-
664 stretching overtone spectra from liquid D_2O between 22 and 152 ^{o}C. Journal of
665 Physical Chemistry, 100(4), 1381-1391.
666 Wigner, E. (1932) On the quantum correction for thermodynamic equilibrium. Physical
667 Review, 40(5), 0749-0759.
668 Wonchoba, S.E., and Truhlar, D.G. (1996) General potential-energy function for H/Ni
669 and dynamics calculations of surface diffusion, bulk diffusion, subsurface-to-
670 surface transport, and absorption. Physical Review B, 53(16), 11222-11241.
671 -. (1998) Embedded diatomics-in-molecules potential energy function for methyl radical
672 and methane on nickel surfaces. Journal of Physical Chemistry B, 102(35), 6842-
673 6860.
674
675

676

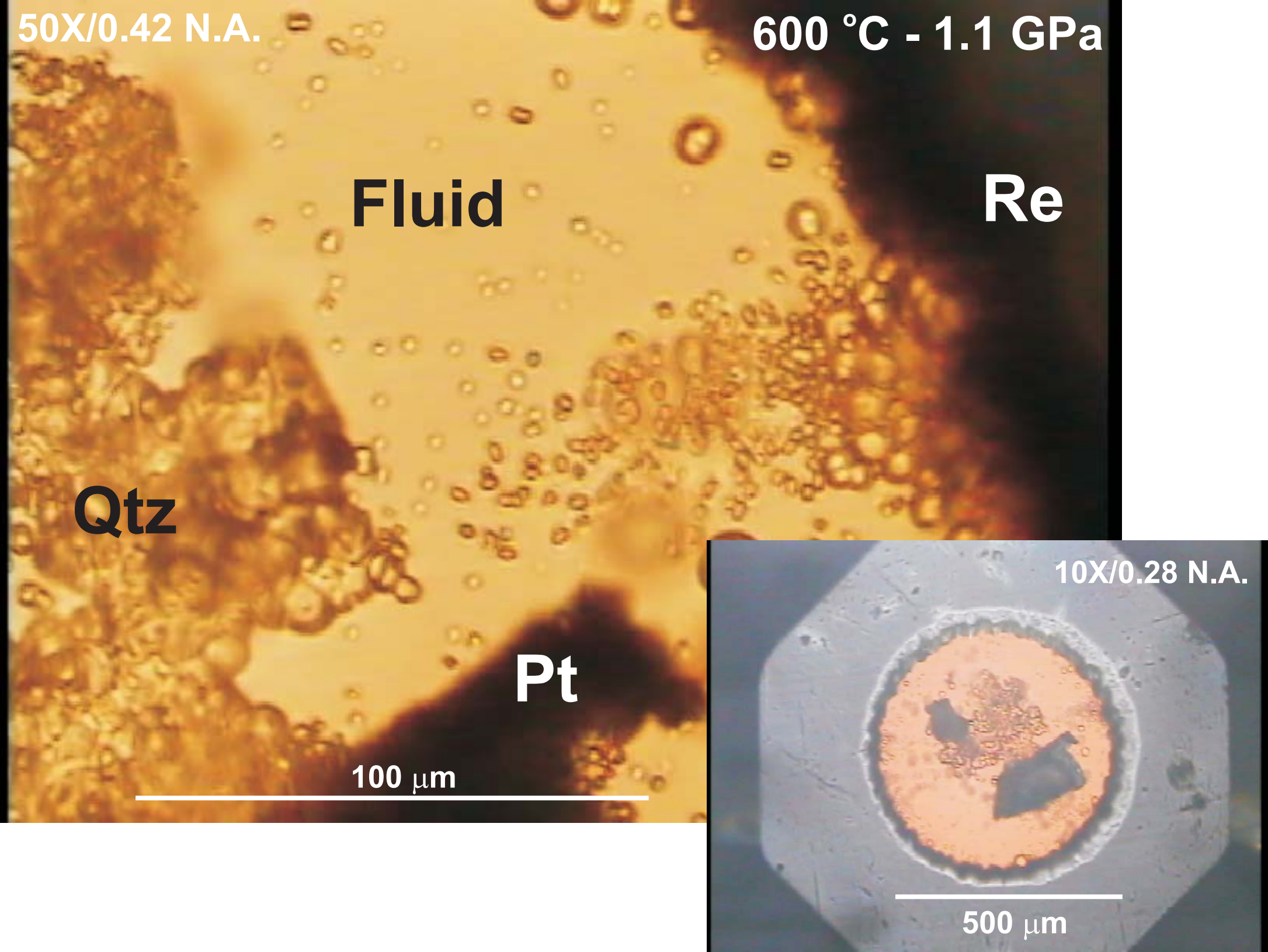
50X/0.42 N.A.
600 °C - 1.1 GPa
Fluid
Re
Qtz
Pt
100 μm
10X/0.28 N.A.
500 μm

a)

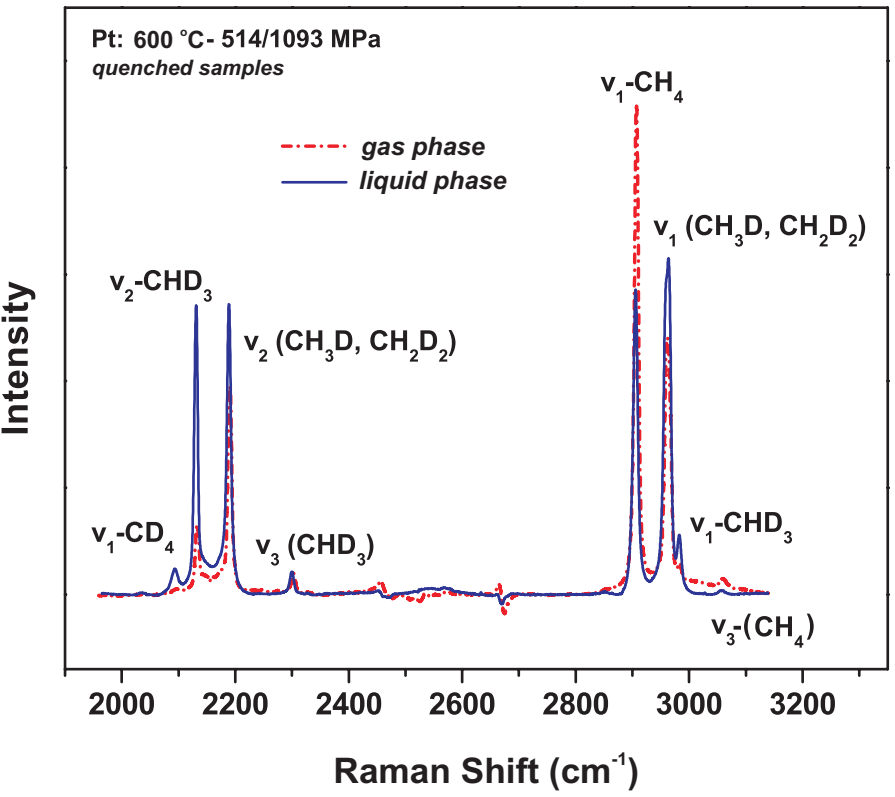
Pt: 600 °C- 514/1093 MPa
quenched samples
gas phase
liquid phase
v1-CH4
v1 (CH3D, CH2D2)
v2-CHD3
v2 (CH3D, CH2D2)
v1-CD4
v3 (CHD3)
v1-CHD3
v3-(CH4)
Intensity
2000
2200
2400
2600
2800
3000
3200
Raman Shift (cm-1)

b)

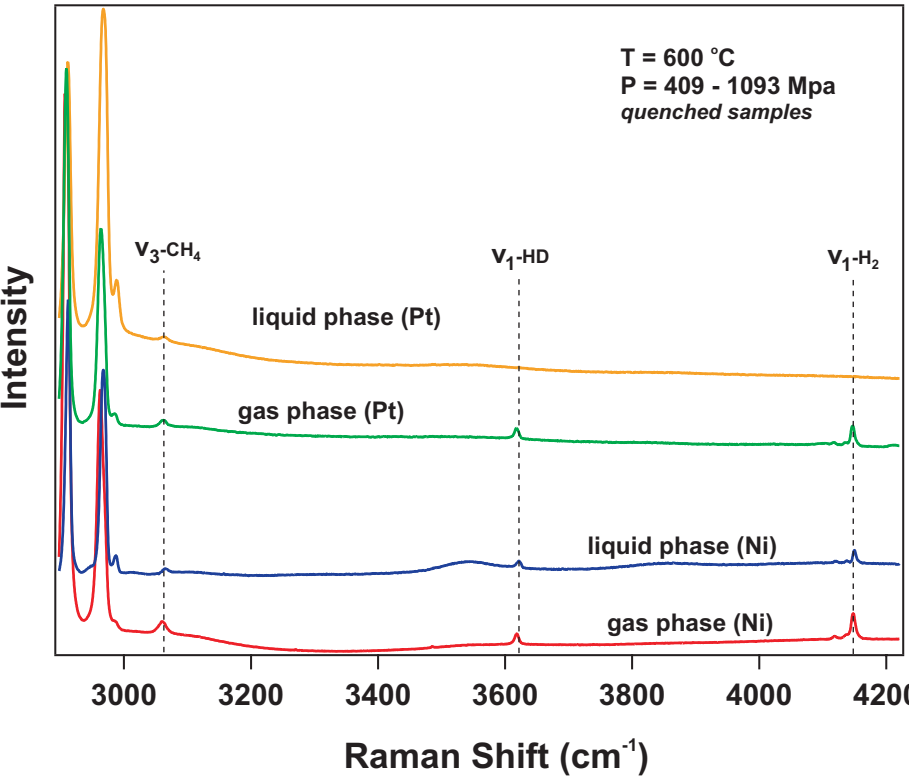
T = 600 °C
P = 409 - 1093 Mpa
quenched samples
v3-CH4
v1-HD
v1-H2
liquid phase (Pt)
gas phase (Pt)
liquid phase (Ni)
gas phase (Ni)
Intensity
3000
3200
3400
3600
3800
4000
4200
Raman Shift (cm-1)

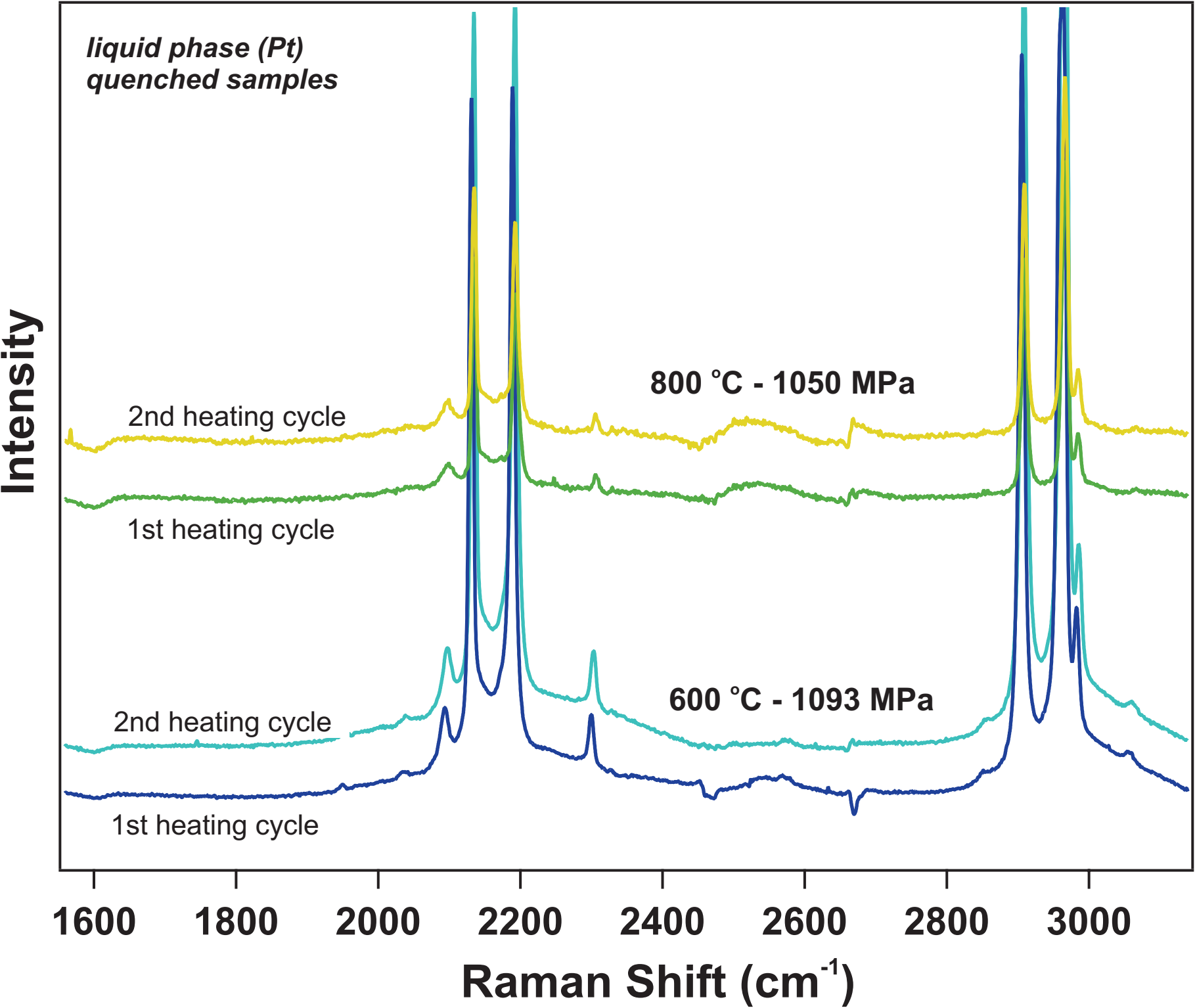
liquid phase (Pt)
quenched samples
800 °C - 1050 MPa
2nd heating cycle
1st heating cycle
600 °C - 1093 MPa
2nd heating cycle
1st heating cycle
Intensity
1600
1800
2000
2200
2400
2600
2800
3000
Raman Shift (cm-1)

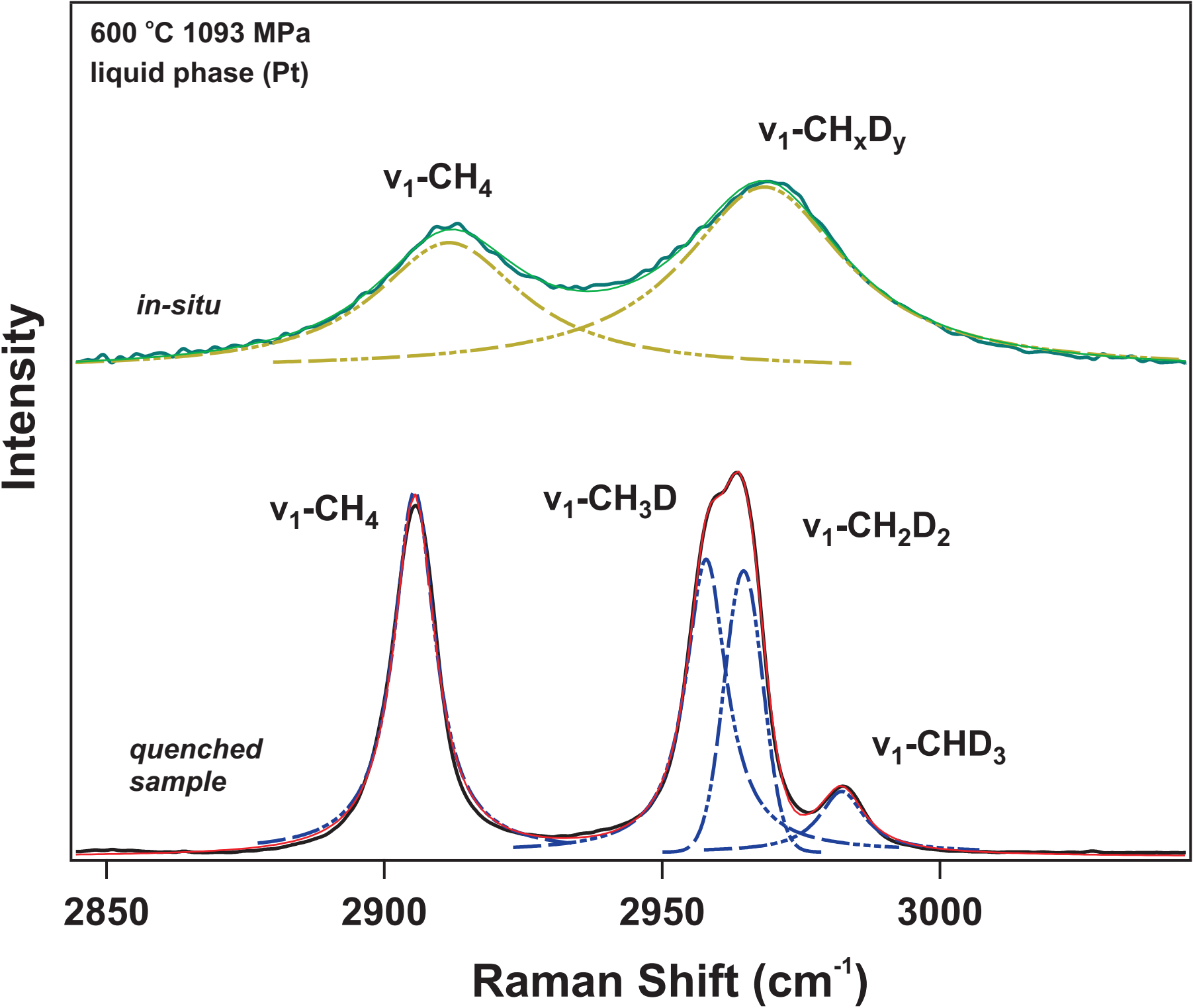
600 °C 1093 MPa
liquid phase (Pt)
v_1-CH_4
v_1-CH_xD_y
in-situ
v_1-CH_4
v_1-CH_3D
v_1-CH_2D_2
v_1-CHD_3
quenched sample
Intensity
2850
2900
2950
3000
Raman Shift (cm^{-1})

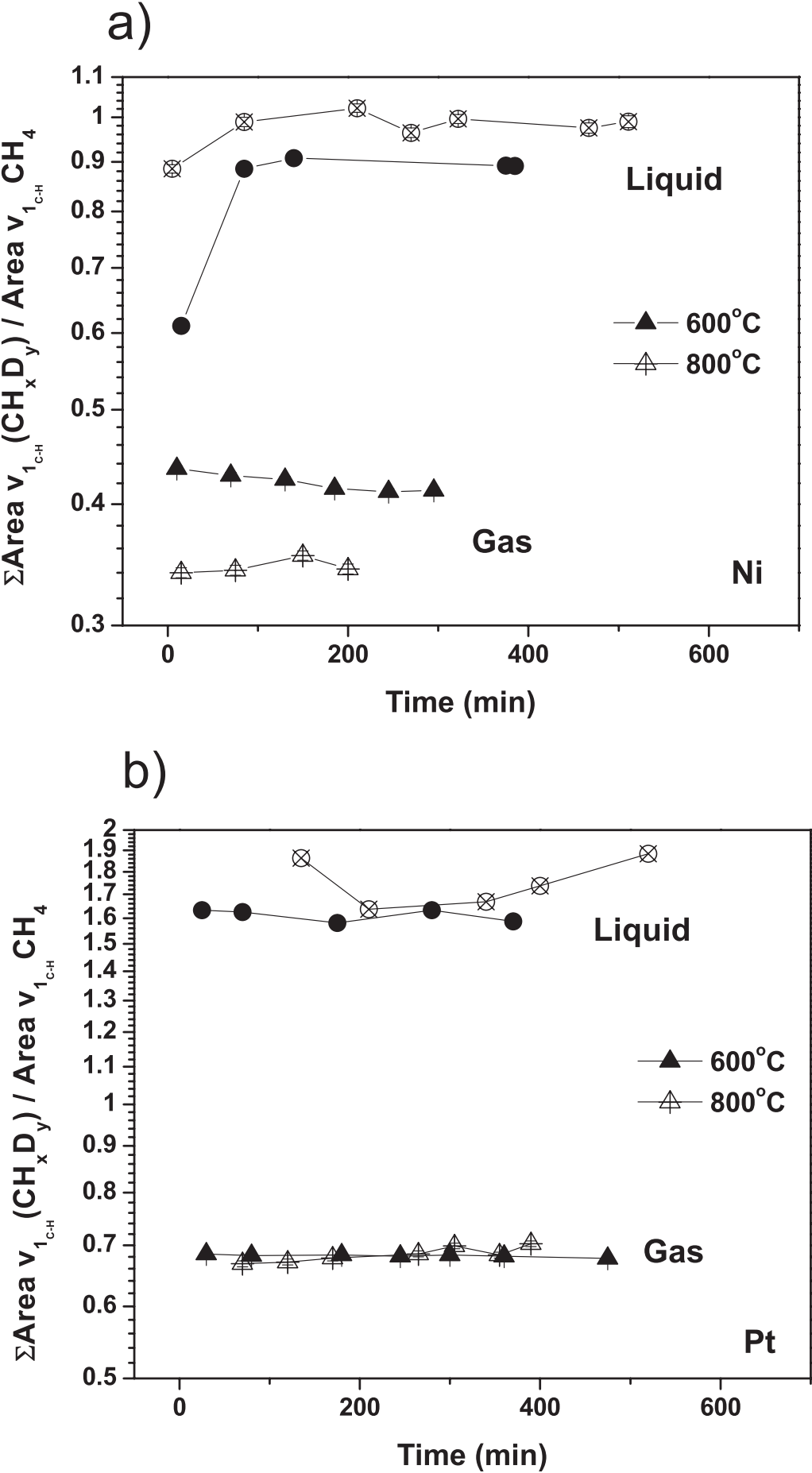
a)
ΣArea ν1C-H (CHxDy) / Area ν1C-H CH4
1.1
1
0.9
0.8
0.7
0.6
0.5
0.4
0.3
Liquid
600°C
800°C
Gas
Ni
0
200
400
600
Time (min)
b)
ΣArea ν1C-H (CHxDy) / Area ν1C-H CH4
2
1.9
1.8
1.7
1.6
1.5
1.4
1.3
1.2
1.1
1
0.9
0.8
0.7
0.6
0.5
Liquid
600°C
800°C
Gas
Pt
0
200
400
600
Time (min)

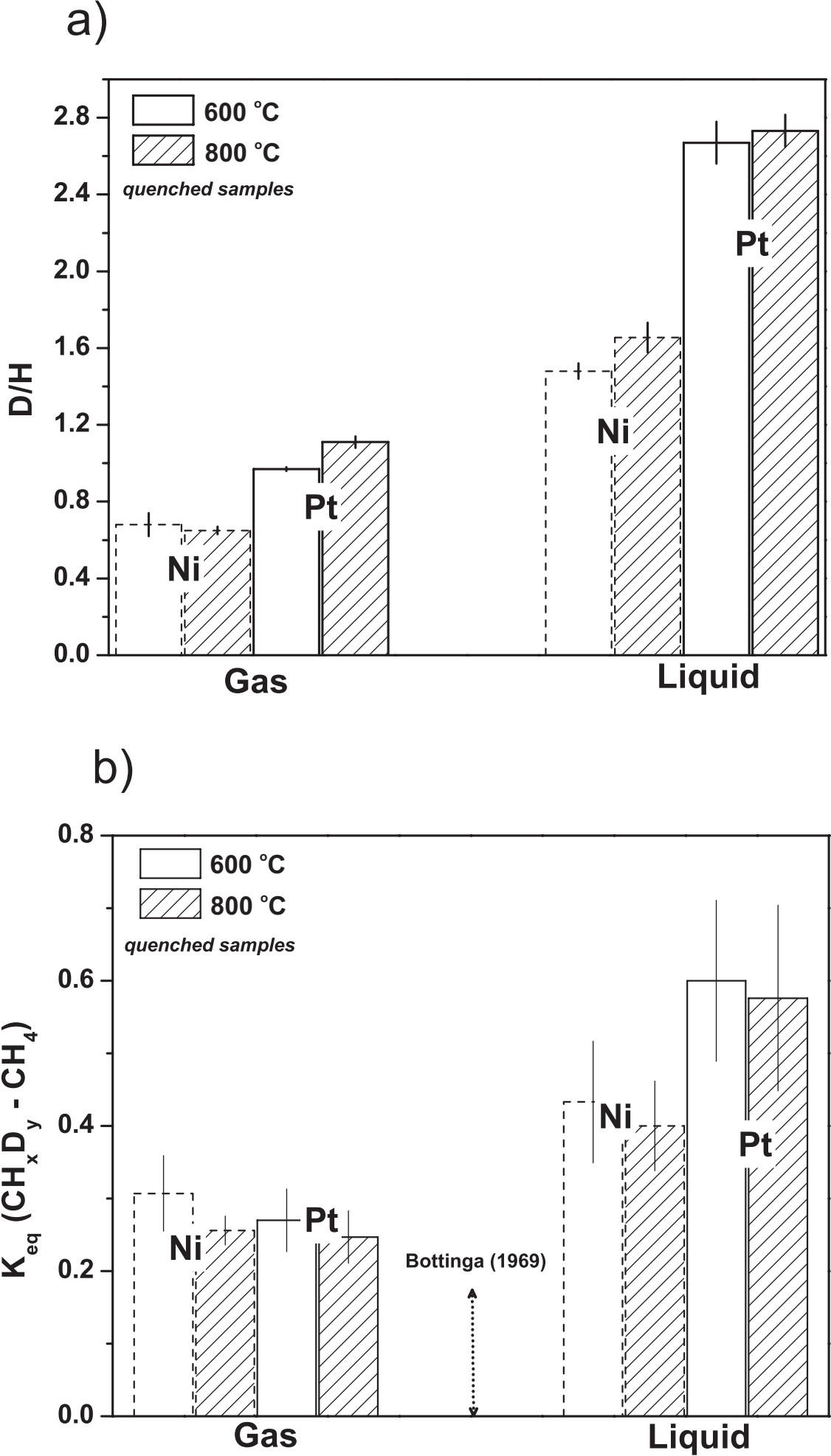
a)
600 °C
800 °C
quenched samples
D/H
2.8
2.4
2.0
1.6
1.2
0.8
0.4
0.0
Ni
Pt
Ni
Pt
Gas
Liquid
b)
600 °C
800 °C
quenched samples
K_{eq} (CH_xD_y - CH_4)
0.8
0.6
0.4
0.2
0.0
Ni
Pt
Bottinga (1969)
Ni
Pt
Gas
Liquid